Nano Research

Open Access

Research Article

Synergistical treatment of TNBC with nanogels via disrupting glycolysis, inducing ICD and ferroptosis

Bixi Sun[1,2], Yiming Qi[1], Haichao Zhu[1], Chenming Zou[1], Zhaozhong Wang[1], Chenfeng Wang[1], Yuepeng Tang[1], Yiyang Xia[3], Derong Cui[3], Zhu Jin[1], Feihu Wang[4], and Shengrong Guo[1] ✉

[1] *School of Pharmaceutic science, Shanghai Jiao Tong University, Shanghai 200240, China*
[2] *SJTU Yazhou Bay Institute of Deepsea Science and Technology, Shanghai Jiao Tong University, Sanya 572024, China*
[3] *Department of Anesthesiology, Shanghai Sixth People's Hospital Affiliated to Shanghai Jiao Tong University School of Medicine, Shanghai 200233, China*
[4] *School of Biomedical Engineering, Shanghai Jiao Tong University, Shanghai 200240, China*

Cite this article: *Nano Research*, **2026**, *19*, 94908349. https://doi.org/10.26599/NR.2026.94908349

ABSTRACT: Triple-negative breast cancer (TNBC) presents formidable therapeutic challenges due to its triple defense system including antioxidant capacity, glycolytic metabolism, and immunosuppressive microenvironment. To overcome these interconnected resistance mechanisms, we developed a multifunctional nanogel (3-in-1 NG) consisting of Fe^{2+}-crosslinked boronate-conjugated mannose-alginate with encapsulated D-*α*-tocopheryl polyethylene glycol succinate (TPGS), which enables efficient tumor delivery. 3-in-1 NG achieved a 52.9% tumor growth inhibition rate and significantly impeded metastatic progression in 4T1 models. Mechanistically, the pH-triggered mannose release led to intracellular accumulation of mannose-6-phosphate. This effectively blocked glycolytic activity and reversed immunosuppressive lactate accumulation, priming tumors for ferroptosis. The nanoplatform simultaneously executes therapeutic functions including metabolic disruption via mannose-mediated glycolysis inhibition, TPGS-induced immunogenic cell death triggering dendritic cell maturation and cytotoxic T-cell infiltration, and Fe^{2+}-dependent lipid peroxidation initiating ferroptosis cascade. These synergistic mechanisms established self-reinforcing therapeutic actions where metabolic inhibition enhanced both immune recognition and ferroptosis susceptibility, creating a feed-forward cycle that progressively dismantled tumor defenses. Our work pioneers a nanomedicine strategy that simultaneously exploits the metabolic plasticity, redox adaptability, and immune escape of TNBC, providing a unified synergistic solution for refractory malignancies.

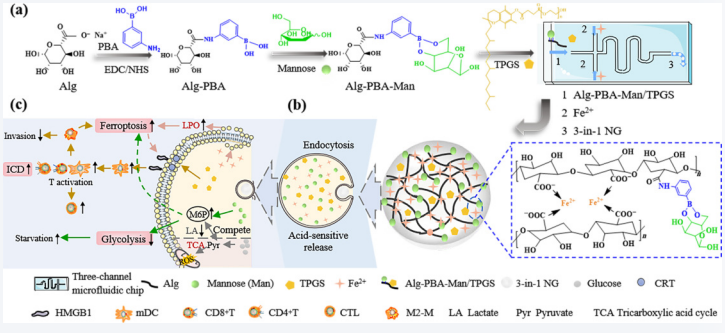

KEYWORDS: three-in-one nanogels, glycolysis disruption, ferroptosis, immunogenic cell death, triple-negative breast cancer

1 Introduction

Triple-negative breast cancer (TNBC) exhibits a metabolic paradox where its glycolytic hyperactivity (Warburg effect) and dysregulated iron metabolism drive aggressiveness yet constitute exploitable vulnerabilities [1–5]. The TNBC metabolic landscape features elevated glucose uptake, transferrin receptor and acyl-CoA synthetase long chain family member 4 (ACSL4) overexpression with ferroportin suppression, and lactate-driven acidosis-features that sustain tumor growth while fostering immunosuppression [6–8]. The metabolic-immunologic crosstalk presents a critical therapeutic opportunity. Mannose has emerged as a potent metabolic disruptor, selectively targeting cancer's glycolytic addiction through conversion to mannose-6-phosphate (M6P), which competitively inhibits hexokinase II (HK2) and phosphoglucose isomerase (PGI) [4, 9–11]. Beyond suppressing proliferation, mannose remodels the tumor microenvironment (TME) by reducing lactate-mediated M2 polarization and enhancing $CD8^+$ T-cell infiltration [12, 13]. However, therapeutic application is hampered by rapid renal clearance and nonspecific distribution [14].

Received: September 3, 2025; **Revised:** December 15, 2025
Accepted: December 15, 2025

✉Address correspondence to srguosjtu@163.com

Complementary to metabolic modulation, D-α-tocopheryl polyethylene glycol succinate (TPGS) induces immunogenic cell death (ICD) via damage-associated molecular pattern (DAMP) release such as calreticulin (CRT), adenosine triphosphate (ATP), and high mobility group box 1 (HMGB1), which stimulate dendritic cell (DC) maturation and subsequent $CD8^+$ T cell activation [15]. Yet, TPGS efficacy is constrained by the immunosuppressive TNBC TME, particularly hypoxia and acidosis from hyperglycolysis [7]. Ferroptosis induction emerges as a third strategic approach, capitalizing on TNBC's inherent iron overload and lipid peroxidation (LPO) susceptibility. Notably, while TNBC cells accumulate iron within ferritin, they maintain limited levels of the labile iron pool (LIP), the catalytically active form required for driving the Fenton reaction [16]. Thus, exogenous delivery of Fe^{2+} via nanogel is designed to strategically expands the LIP and triggers potent ferroptotic cascades [12, 17].

The interconnected nature of these pathways reveals a metabolic disruption reduces lactate production, alleviating powerful therapeutic synergy: glycolysis inhibition, evidenced by reduced lactate production, contributes to remodeling the immunosuppressive TME, while the consequent metabolic stress synergizes with Fe^{2+} to potentiate ferroptosis. The interplay helps establish a therapeutic context favorable for the concurrent induction of ICD and ferroptosis [18, 19]. Mannose-mediated metabolic disruption impairs reduced nicotinamide adenine dinucleotide phosphate (NADPH) regeneration, dramatically sensitizing tumor cells to Fe^{2+}-driven LPO and ferroptosis. The potent DAMPs released during the process can override initial immunosuppression effects, resulting in net activation of antitumor immunity [4, 20]. Concurrently, TPGS-induced ICD generates tumor antigens that synergize with ferroptosis-derived damage signals to amplify antitumor immunity [15]. This creates a self-reinforcing action where metabolic modulation enhances both immune activation and ferroptosis sensitivity, which in turn further disrupt glycolysis [21–23].

To harness this synergy, we engineered a 3-in-1 nanogel (3-in-1 NG) via microfluidic assembly of borate ester-conjugated mannose for pH-responsive glycolysis inhibition, Fe^{2+} crosslinkers for ferroptosis induction, and encapsulated TPGS for ICD (Fig. 1). The nanogel achieves tumor-selective accumulation via the enhanced permeability and retention (EPR) effects and active uptake. Following internalization, the acidic pH (approximately 5.5) of endosomal or lysosomal compartments trigger controlled release of the therapeutic payloads. The nanogel establishes a self-amplifying therapeutic action: metabolic rewiring enhances ferroptosis sensitivity and immune activation, which reciprocally amplify metabolic disruption [24]. Further studies have confirmed that the system can down-regulate B-cell lymphoma-2 (BCL-2) expression, activate apoptotic pathways, and reduce lactate production. Our design simultaneously addresses the key therapeutic challenges of TNBC-poor tumor specificity, rapid clearance, and monotherapy resistance while demonstrating excellent biosafety [10, 25–27]. The work provides an example for the next generation of jointly exploiting metabolic, redox, and immunological vulnerabilities to treat refractory cancers.

2 Experimental

2.1 Materials, cells, and animals

Sodium alginate (Alg, 1% viscosity 1000–1200 mPa·s, mannuronate/guluronate ~ 1, verified by Fourier transform infrared (FT-IR) spectroscopy in Fig. S1 and Table S1 in the Electronic Supplementary Material (ESM)) [28]. Key reagents including D-mannose, calcium chloride, 3-aminobenzoboric acid (PBA), 1-ethyl-3-(3-dimethylaminopropyl) carbodiimide hydrochloride (EDC), N-hydroxysuccinimide (NHS), TPGS, and $FeSO_4{\cdot}7H_2O$ were purchased from Macklin, Aladdin, and Sinopharm (Shanghai, China). Cell culture reagents including Dulbecco's modified eagle medium (DMEM), Roswell Park Memorial Institute medium (RPMI 1640), fetal bovine serum (FBS), trypsin, Penicillin-Streptomycin, and phosphate-buffered saline (PBS) were sourced from Thermo Fisher (USA), ExCell (Suzhou, China), Biosharp (Anhui, China), and Beyotime (Shanghai, China). Matrigel was from Corning (USA). Assay kits for cell viability (cell counting kit-8 (CCK-8)), apoptosis detection (Annexin V-FITC), cytokine measurement (tumor necrosis factor-α (TNF-α); interferon-γ (IFN-γ); interleukin-6 (IL-6); transforming

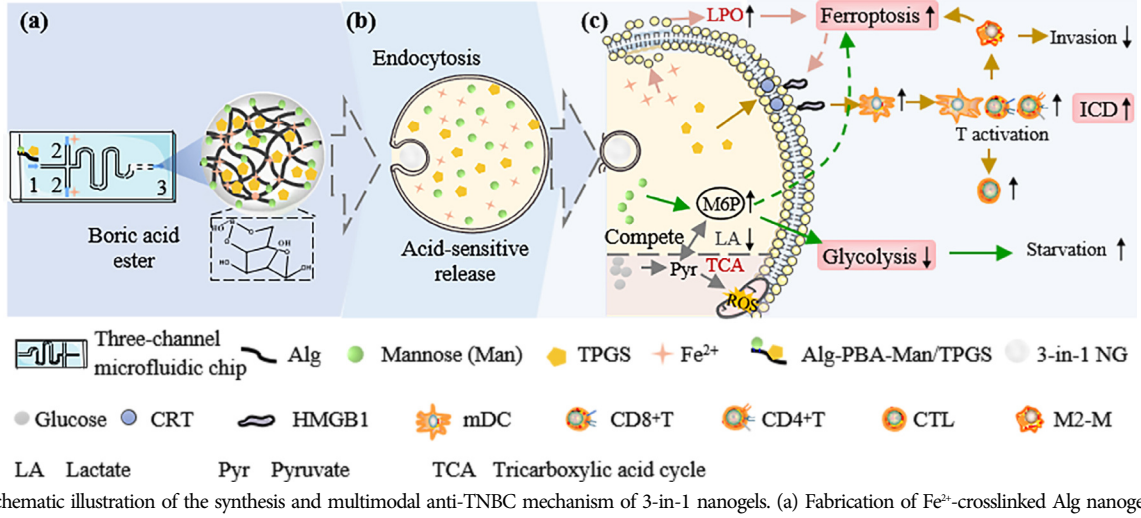

Figure 1 Schematic illustration of the synthesis and multimodal anti-TNBC mechanism of 3-in-1 nanogels. (a) Fabrication of Fe^{2+}-crosslinked Alg nanogels co-loaded with TPGS (via encapsulation) and mannose (via pH-sensitive borate ester bonds) using a custom three-channel microfluidic chip. (b) Tumor microenvironment-responsive release of all components. (c) Synergistic therapeutic mechanisms: Fe^{2+}-mediated LPO induces ferroptosis; mannose metabolism-triggered M6P accumulation suppresses glycolysis; and TPGS-driven ICD via DAMP release promotes DC maturation and cytotoxic T lymphocyte (CTL) infiltration. The integrated strategy concurrently enhances ferroptosis, impairs tumor growth, and activates anti-tumor immunity for potent TNBC therapy.

growth factor-β (TGF-β) enzyme-linked immunosorbent assay (ELISA) kits), metabolic analysis (M6P; fructose-1,6-bisphosphate (FDP); lactate), ferroptosis analysis (BODIPY 581/591 C11; total antioxidant capacity test kit, 2,2'-azino-bis(3-ethylbenzothiazoline-6-sulfonic acid (ABTS); total iron), and ICD evaluation (CRT antibody, HMGB1, ATP, reactive oxygen species (ROS)) were sourced from Thermo Fisher, Beyotime, and other specialized suppliers. Critical antibodies for flow cytometry (CD markers) and western blotting (WB; signal transducer and activator of transcription 1 (STAT1); STAT6; nuclear factor κ-light-chain-enhancer of activated B cells p65 subunit (NF-κB p65); inhibitor of $\kappa B\alpha$ (I$\kappa B\alpha$); glutathione peroxidase 4 (GPX4); ACSL4; BCL-2-like protein 1 (BCL-XL); myeloid cell leukemia-1 (MCL-1)) were obtained from Elabscience and Abcam (Shanghai, China).

The murine TNBC cell line 4T1-luc (luciferase-expressing), RAW 264.7 macrophages, and fibroblast L929 cells were maintained in-house. 4T1-luc cells were cultured in RPMI-1640 supplemented with 10% FBS and 1% Penicillin-Streptomycin, while RAW 264.7 and L929 cells were maintained in DMEM under standard conditions (37 °C, 5% CO_2). For *in vivo* studies, female BALB/c mice (3–4 weeks old, 17–20 g) were obtained from Sipei Fu (Suzhou, China) and housed in a specific pathogen-free (SPF) conditions with controlled temperature (22 ± 1 °C), humidity (50% ± 5%), and 12 h light/dark cycles. All experimental procedures were conducted in strict accordance with the National Institutes of Health's Guide for the Care and Use of Laboratory Animals (NIH Publication No. 80-23, revised 1996) and approved by the Institutional Animal Care and Use Committee of Shanghai Jiao Tong University (Approval No. 2024-01-LY-CDR-111), following Animal Research: Reporting of *In Vivo* Experiments (ARRIVE) guidelines for reporting animal research.

2.2 Preparation of the 3-in-1 NG

3-in-1 nanogels were prepared through a sequential conjugation and microfluidic synthesis process. First, Alg was functionalized with PBA via EDC/NHS-mediated coupling in deionized water (pH 5.5) at a molar ratio of 4:1:1:1 (Alg carboxyl group: PBA: EDC: NHS), forming covalent amide bonds between Alg and PBA [29, 30]. Following conjugation, mannose (Alg carboxyl group: mannose = 4:1) was introduced to form borate ester bonds with Alg-PBA, and the resulting Alg-PBA-Man conjugate was thoroughly purified by dialysis (molecular weight cut-off; MWCO 2500 Da) for 72 h with 6 dialysate changes per day to remove urea byproducts, unreacted EDC/NHS, PBA-NH_2, and mannose. The purity of the conjugate was verified by ultraviolet–visible (UV–vis) spectroscopy, which showed no residual aromatic impurities in the 260–280 nm range and only the characteristic PBA absorption. Subsequently, TPGS was incorporated into the Alg-PBA-Man matrix via hydrophobic interactions, followed by dialysis under identical conditions to remove unincorporated TPGS, yielding a precursor solution for microfluidic synthesis (Fig. 2(a)) [31–33].

For nanogel formation, a three-channel microfluidic device was employed under optimized conditions (Fig. 2(b) and Fig. S2 in the ESM). The Alg-PBA-Man/TPGS precursor solution (1 mg/mL, 2 mL) was injected through the central channel, while Fe^{2+} solution (0.2 mg/mL, 20 mL) was delivered through the two side channels using a dual-channel pump (Longer Pump, UK), enabling instantaneous crosslinking at the junction to form uniform nanogels. Using this methodology, nanogels including Fe^{2+}-Alg nanogels (NG), Fe^{2+}-Alg/TPGS nanogels (2 NG-1), and Fe^{2+}-Alg-PBA-Man nanogels (2 NG-2) were similarly prepared for comparative studies. All nanogels were synthesized using deoxygenated ultrapure water (boiled and cooled under inert atmosphere), and freshly prepared formulations were employed for all experiments to minimize oxidation during preparation.

2.3 Characterization of the 3-in-1 NG

The chemical structure of the freeze-dried Alg-PBA-Man conjugate was verified by FT-IR spectroscopy (Thermo Fisher Scientific, USA) with scans ranging from 4000 to 400 cm^{-1}. Nanogel size distribution and zeta potential were measured by dynamic light scattering (DLS; Zetasizer Nano, Malvern Panalytical, UK), while morphological features were examined using scanning electron microscopy (SEM; Thermo Fisher Scientific, USA) for lyophilized hydrogels and transmission electron microscopy (TEM; Thermo Fisher Scientific, USA) for the 3-in-1 NG. The *in situ* gelation capability was assessed by injecting 3-in-1 NG solution (mixed with ink for visualization) and deionized water as a control into a 1.8 mM Ca^{2+} solution, with gel formation recorded at 0 min, 1 min, 0.5 h, and 2 h. Rheological properties were analyzed using a rheometer (TA Instruments, USA) by measuring storage (G') and loss (G") moduli under varying shear rates, stresses, and time. Frequency scans (0.1–100 rad/s), time sweeps (0–200 s), and amplitude tests (1 rad/s, 0.2% strain) were performed to assess viscoelastic behavior. The colloidal stability of the nanogels was monitored over 7 days at 4 °C by measuring changes in particle size, polydispersity index (PDI), and zeta potential. Additionally, the stability of Fe^{2+} within the nanogel matrix was examined by quantifying Fe^{2+} concentration using the o-phenanthroline method [34] and total iron content with a commercial assay kit, from which the Fe^{2+} retention rate was calculated over 5 days.

2.4 *In vitro* pH-responsive release study

The pH-responsive release profiles of mannose, TPGS, and Fe^{2+} from the 3-in-1 NG were investigated using a dialysis method. The nanogel solution was placed in dialysis bags (MWCO 2500 Da) and immersed in buffer solutions at pH 7.4, 6.5, and 5.5. The systems were incubated at 37 °C under continuous shaking at 100 rpm (Minquan, China), and samples were collected at predetermined time intervals over 108 h. To maintain sink conditions, an equal volume of fresh corresponding buffer was supplemented after each sampling. Released mannose was quantified at 498 nm via the DNS colorimetric method [35], ferrous ions at 510 nm via the o-phenanthroline method, and TPGS at 202 nm via ultraviolet–visible spectroscopy (UV–vis; Hitachi, Japen). Cumulative release percentages were calculated from pre-established standard curves (Figs. S2(c)–S2(e) in the ESM).

2.5 Cellular uptake assay

The cellular uptake efficiency of 3-in-1 NG was evaluated in 4T1 cells during logarithmic growth phase. After overnight adhesion in culture plates, cells were incubated with fluorescein isothiocyanate (FITC)-labeled 3-in-1 NG for predetermined time intervals (0–2 h) at 37 °C under 5% CO_2. Following incubation, cells were thoroughly washed with PBS to remove non-internalized nanogels. Cellular uptake was qualitatively analyzed by fluorescence microscopy (IX73, Olympus, Japan) and quantitatively measured using flow cytometry (Fortessa X20, BD Biosciences, USA) after trypsin-mediated cell detachment.

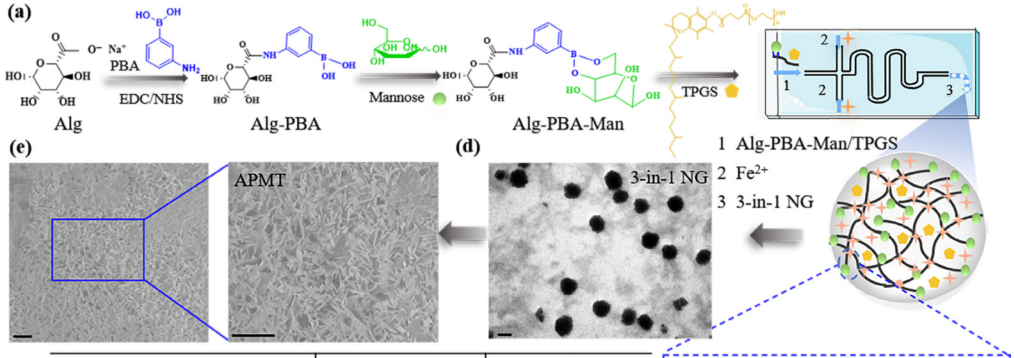

(c)

Nanogel	Mannose			TPGS			Fe^{2+}		
	C (μg/mL)	EE (%)	LC (%)	C (μg/mL)	EE (%)	LC (%)	C (μg/mL)	EE (%)	LC (%)
NG	-	-	-	-	-	-	4.9	89.8	3.3
2 NG-1	-	-	-	10.1	78.8	6.8	4.8	87.5	3.1
2 NG-2	10.6	71.3	6.8	-	-	-	4.7	86.5	3.2
3-in-1 NG	10.8	85.9	6.7	10.3	77.9	8.4	4.8	88.2	4.0

(b) Optimization of the formulation using microfluidics

	Formulation	Alg concentration (mg/mL)	Fe^{2+} concentration (mg/mL)	Aqueous phase 1/2 (V/V)	1 flow rate (mL/min)	2 flow rate (mL/min)	FR	Size (nm)	PDI
FR	F1	1.00	0.20	1/20	0.14	1.35	0.05	200.0 ± 6.97	0.3 ± 0.05
	F2	1.00	0.20	1/10	0.30	1.35	0.11	202.67 ± 3.72	0.222 ± 0.011
	F3	1.00	0.20	1/5	0.68	1.35	0.25	223.57 ± 3.56	0.58 ± 0.04
Flow rates	F4	1.00	0.20	1/10	0.63	2.85	0.11	134.4 ± 7.3	0.367 ± 0.067
	F5	1.00	0.20	1/10	0.13	0.60	0.11	129.9 ± 5.73	0.396 ± 0.023
Alg concentration	F6	0.50	0.20	1/10	0.30	1.35	0.11	159.4 ± 8.69	0.244 ± 0.041
	F7	2.00	0.20	1/10	0.30	1.35	0.11	628.3 ± 16.84	0.539 ± 0.034
Fe^{2+} concentration	F8	1.00	0.20	1/10	0.30	1.35	0.11	152.3 ± 3.736	0.321 ± 0.025
	F9	1.00	1.00	1/10	0.30	1.35	0.11	544.1 ± 28.626	0.461 ± 0.023

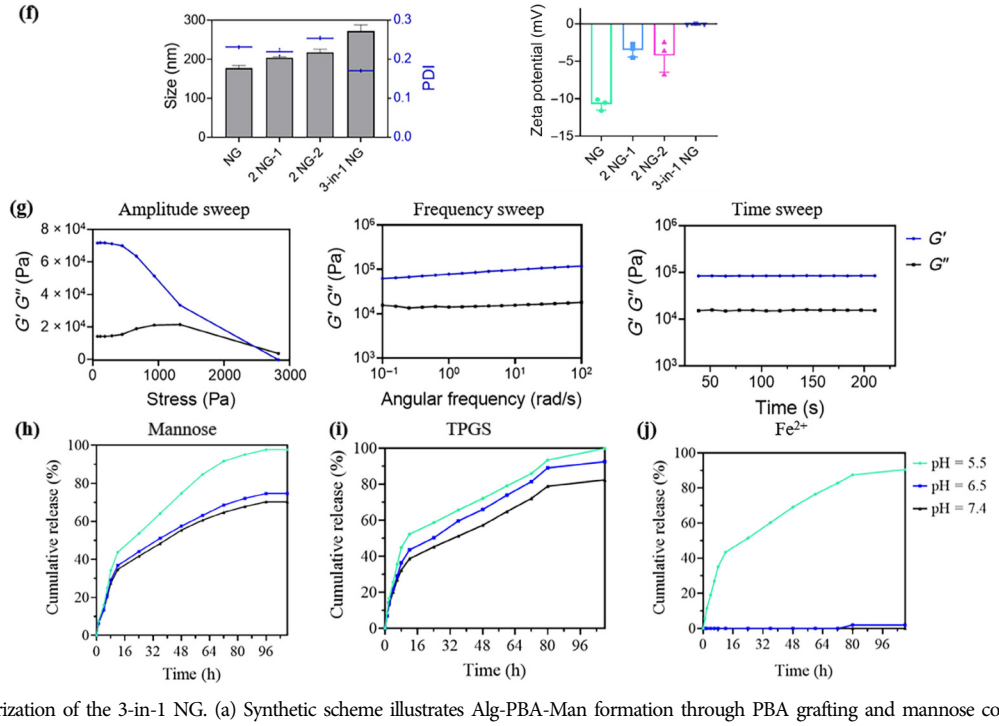

Figure 2 Characterization of the 3-in-1 NG. (a) Synthetic scheme illustrates Alg-PBA-Man formation through PBA grafting and mannose conjugation, followed by TPGS incorporation, with subsequent nanogel preparation using a three-channel microfluidic chip. (b) Optimization of microfluidic parameters for nanogel formation. (c) Concentration of constituents, EE, and LC of each nanogel. (d) TEM image of the spherical 3-in-1 NG (scale bar: 100 nm). (e) SEM images of Alg-PBA-Man/TPGS hydrogel (scale bars: 10 μm). (f) Hydrodynamic size, PDI, and zeta potential of NG, 2 NG-1, 2 NG-2, and 3-in-1 NG. (g) Rheological properties of the 3-in-1 NG hydrogel, including strain sweep ($G' > G''$ below 2450 Pa), frequency-independent viscoelasticity, and time-dependent stability. Release curves of (h) mannose, (i) TPGS and (j) Fe^{2+} in the 3-in-1 NG. Data are represented as mean ± SD ($n = 5$).

2.6 Cell viability assay

The cytotoxicity of the formulations was evaluated in logarithmically growing 4T1 cells seeded in 96-well plates (5×10^3 cells/well). After overnight adhesion, cells were treated with fresh medium containing different concentrations of TPGS (1.3–10.3 μg/mL), mannose (1.4–10.8 μg/mL), Fe^{2+} (0.6–4.8 μg/mL), NG-2 (Ca^{2+}-Alg-PBA-Man nanogels, 1.4–10.8 μg/mL mannose equivalent), NG-3 (Ca^{2+}-Alg/TPGS nanogels, 1.3–10.3 μg/mL TPGS equivalent), NG-4 (Ca^{2+}-Alg-PBA-Man/TPGS nanogels, 1.4–10.8 μg/mL mannose equivalent), NG (0.6–4.8 μg/mL Fe^{2+} equivalent), 2 NG-1 (1.3–10.3 μg/mL TPGS equivalent), 2 NG-2 (1.4–10.8 μg/mL mannose equivalent), and 3-in-1 NG (1.4–10.8 μg/mL mannose equivalent). Following 24 h incubation, cell viability was assessed using CCK-8 assay, with absorbance measured at 450 nm after 2 h reagent incubation. To evaluate the safety profile, normal murine fibroblast L929 cells were treated under identical conditions using the highest concentration of each formulation tested in the 4T1 cell experiments, with viability assessed via the same CCK-8 protocol.

2.7 Cell apoptosis assay

Apoptosis in 4T1 cells was analyzed via flow cytometry with an Annexin V-FITC staining kit. In brief, adherent cells undergoing logarithmic growth were subjected to a 24 h treatment with PBS, 2 NG-1, 2 NG-2, or 3-in-1 NG. After treatment, the cells were harvested and stained according to the manufacturer's protocol for quantitative analysis.

2.8 Cell migration and invasion assays

The anti-migratory and anti-invasive effects of the 3-in-1 NG were investigated using scratch wound healing and Transwell assays. In the scratch assay, confluent monolayers of 4T1 cells were mechanically wounded and assigned to four treatment conditions: serum-free medium with PBS (control), serum-free medium with 3-in-1 NG, serum-free medium containing 40 mM lactate with PBS, and serum-free medium containing both 40 mM lactate and 3-in-1 NG. Wound closure was monitored by capturing images at 0 and 24 h post-scratching using an inverted microscope (Olympus, Japan), with wound areas quantified from five randomly selected fields per group.

For the Transwell migration assay, 4T1 cells suspended in serum-free medium (with PBS or 3-in-1 NG) were seeded into the upper chambers with 8-μm pores, while the lower chambers contained complete medium with or without 40 mM lactate as a chemoattractant. After 24 h of incubation, non-migrated cells were removed, and migrated cells on the lower membrane surface were fixed with 4% paraformaldehyde, stained with 0.1% crystal violet, and quantified microscopically from five random fields per insert. The invasion assay was performed similarly, except that the upper chambers were pre-coated with Matrigel to mimic the extracellular matrix, and invading cells were quantified after 24 h using the same staining and imaging protocol.

2.9 Fenton reaction biomarker assays

The Fenton reaction activity of 3-in-1 NG was evaluated through LPO and total antioxidant capacity measurements at both cellular and animal levels [36]. For cellular assays, adherent 4T1 cells were treated with PBS, Fe^{2+}, NG, 2 NG-2, or 3-in-1 NG for 24 h. LPO was assessed using BODIPY 581/591 C11 staining (1 h, 37 °C), followed by fluorescence microscopy imaging and quantitative flow cytometry analysis. Intracellular antioxidant capacity was determined via ABTS assay.

In vivo evaluation utilized tumor tissues from five treatment groups (control, mannose, 2 NG-1, 2 NG-2, and 3-in-1 NG). Tissue homogenates were prepared by ultrasonic disruption for simultaneous measurement of total antioxidant capacity (ABTS assay) and iron ion content (colorimetric assay).

2.10 Glycolysis biomarker assays

The glycolytic inhibitory effect of 3-in-1 NG was systematically evaluated by quantifying key metabolic intermediates (M6P, FDP, and lactate) in both cellular and animal models [4, 37, 38]. For *in vitro* analysis, adherent 4T1 cells were treated with PBS, mannose, Ca^{2+} cross-linked Alg nanogels (NG-1), NG, 2 NG-2, or 3-in-1 NG for 24 h, followed by ultrasonic lysis (Bioruptor Pico, Japan) and subsequent measurement of M6P, FDP, and lactate levels using specific commercial assay kits.

In vivo assessment was performed using tumor tissues from 4T1-bearing mice across five treatment groups (control, mannose, 2 NG-1, 2 NG-2, and 3-in-1 NG). Tissue homogenates were prepared through mechanical homogenization and ultrasonic disruption, with metabolite concentrations determined using the same standardized assay kits.

2.11 ICD biomarker assays

The induction of ICD by 3-in-1 NG was comprehensively evaluated through multiple biomarkers at cellular and animal levels [15, 39]. *In vitro* studies using 4T1 cells treated with PBS, TPGS, 2 NG-1, or 3-in-1 NG for 24 h demonstrated ICD through four key parameters: CRT exposure was analyzed by immunofluorescence staining (anti-CRT primary and Alexa Fluor 488-conjugated secondary antibodies) followed by fluorescence microscopy and flow cytometry; extracellular HMGB1 release was quantified by ELISA; ATP secretion was measured using a commercial assay kit; and intracellular ROS generation was detected using 2',7'-Dichlorodihydrofluorescein diacetate (DCFH-DA) with kinetic fluorescence measurements.

In vivo validation was performed in 4T1 tumor-bearing mice across five treatment groups (saline, mannose, 2 NG-1, 2 NG-2, and 3-in-1 NG). Tumor sections were processed for CRT immunofluorescence analysis (including fixation, embedding, antigen retrieval, and antibody staining), while tissue supernatants were assessed for HMGB1 release using ELISA.

2.12 Animal experiments and therapeutic evaluation

An orthotopic breast cancer model was established by injecting 4T1-luc cells (2×10^5 cells in 100 μL PBS) into the fourth mammary fat pad of female BALB/c mice using a 29-gauge insulin syringe. Tumor progression was monitored daily by bioluminescence imaging until volumes reached 100 ± 10 mm^3 (7–10 days post-implantation), at which point mice were randomized into five treatment groups (n = 7/group): saline control, mannose, 2 NG-1, 2 NG-2, and 3-in-1 NG. Treatments were administered intratumorally (50 μL/injection) every 5 days (days 15, 20, and 25).

Tumor dimensions and body weights were measured every 2 days for volume calculation and growth inhibition analysis, supplemented by *in vivo* imaging system (IVIS) imaging every 6 days. Upon study completion (days 25–30), tumors and major organs (heart, liver, spleen, lungs, kidneys) were harvested for histopathological evaluation. Tumor sections underwent

hematoxylin and eosin (H&E) staining and terminal deoxynucleotidyl transferase dUTP nick end labeling (TUNEL) apoptosis detection, while organ sections were processed for H&E staining to assess systemic toxicity. To assess potential iron toxicity, serum Fe^{2+} concentrations were measured in mice following treatment. The overall iron metabolic balance was further verified through serum ferritin quantification.

2.13 Western blotting analysis

WB analysis was performed to investigate the mechanisms underlying 3-in-1 NG-induced macrophage repolarization from M2 to M1 phenotype and its regulatory effect on ferroptosis- and apoptosis-related protein expression in tumor tissues. *In vitro*, RAW 264.7 macrophages were first polarized to the M2 phenotype with IL-4, with LPS/IFN-γ serving as the M1 control. To explore the involvement of the NF-κB and STAT1 pathways, M2 macrophages were pretreated with the NF-κB inhibitor BAY 11-7082 (5 μM) or the STAT1 inhibitor Fludarabine (50 μM) for 1 h prior to 3-in-1 NG stimulation. Protein levels of key signaling molecules, including STAT1 (ab230428, 1:1,000), phospho-STAT1 (Tyr727; ab109461, 1:1,000), STAT6 (ab263947, 1:1,000), phospho-STAT6 (Tyr641; ab263947, 1:1,000), NF-κB p65 (ab76302, 1:1,000), phospho-NF-κB p65 (Tyr536; ab76302, 1:1,000), IκBα (ab32518, 1:1,000), and phospho-IκBα (Tyr32; ab92700, 1:1,000) were assessed using specific antibodies. *In vivo*, tumor tissues from 4T1-bearing mice treated with saline, mannose, 2 NG-1, 2 NG-2, or 3-in-1 NG were homogenized, and proteins were extracted for immunoblotting. Membranes were probed with antibodies against GPX4 (ab125066, 1:1,000), ACSL4 (ab155282, 1:1,000), MCL-1 (ab32087, 1:1,000), and BCL-XL (ab32370, 1:1,000), followed by incubation with horseradish peroxidase (HRP)-conjugated secondary antibodies, and protein bands were visualized using enhanced chemiluminescence.

2.14 Immune cell profiling by flow cytometry

The immunomodulatory effects of 3-in-1 NG were evaluated through comprehensive immune cell analysis of lymph nodes and tumor tissues from treated 4T1 tumor-bearing mice (saline, mannose, 2 NG-1, 2 NG-2, and 3-in-1 NG groups). Single-cell suspensions were prepared by mechanical dissociation and 70 μm filtration, followed by multicolor flow cytometry analysis using antibody panels: for DCs in tumor-draining lymph nodes (TDLNs) and tumors (anti-APC-CD11c, anti-FITC-CD80, anti-PE-CD86), for T cell subsets (anti-APC-CD45, anti-PE/Cy5.5-CD3, anti-PE-CD8α, anti-FITC-CD4), and for macrophage polarization (anti-FITC-CD11b, anti-APC-F4/80, anti-PE-CD86, anti-PE/Cy7-CD206).

2.15 Cytokine secretion detection assay

The immunomodulatory effects of different treatments were further characterized by quantifying key cytokines (TNF-α, IFN-γ, IL-6, and TGF-β) in tumor tissues using commercial ELISA kits.

2.16 Statistical analysis

All experimental data were analyzed using GraphPad Prism 8.0 (GraphPad Software, USA) and presented as mean ± standard deviation (SD) from biological replicates. Multiple-group comparisons were performed using one-way ANOVA followed by Tukey's post-hoc test, with statistical significance thresholds established as $^{*}P < 0.05$, $^{**}P < 0.01$, $^{***}P < 0.001$, and $^{****}P < 0.0001$ to determine treatment effects across all experimental groups.

3 Results and discussion

3.1 Preparation and characterization of 3-in-1 NG

3-in-1 NG was synthesized through a multi-step assembly process involving EDC/NHS-mediated grafting of PBA onto Alg chains, followed by mannose conjugation via reversible PBA-diol interactions (Fig. 2(a)). The PBA grafting rate in Alg-PBA-Man was determined to be 20.03% ± 0.62%, corresponding to approximately one PBA moiety per five Alg structural units — a density that ensures effective dynamic boronic acid-diol binding while providing sufficient structural anchors for subsequent Fe^{2+}-mediated coordination crosslinking. FT-IR analysis confirmed successful functionalization, showing characteristic B-O vibration bands (1360–1400 cm^{-1}) from PBA and typical carbohydrate signatures (1000–1200, 897 cm^{-1}) from mannose (Fig. S1 in the ESM).

Nanogel formation was achieved using an optimized three-channel microfluidic chip (Fig. 2(b) and Fig. S2 in the ESM), where Alg-PBA-Man/TPGS core flow was sheathed by Fe^{2+} solution to initiate crosslinking through a mechanism involving Fe^{2+}-Alg coordination followed by secondary nucleation [32]. The resulting 3-in-1 NG exhibited high encapsulation efficiencies (EEs) of 85.9%, 77.9%, and 88.2% for mannose, TPGS, and Fe^{2+}, respectively, with corresponding loading capacities (LCs) of 6.7%, 8.4%, and 4.0% (Fig. 2(c)). Following synthesis, all nanogel formulations were uniformly dispersed in an aqueous Alg solution. The common preparation enabled Ca^{2+}-triggered *in situ* gelation for each group upon intratumoral injection, leveraging the physiological Ca^{2+} present within the tumor milieu. *In vitro*, exposure to 1.8 mM Ca^{2+} prompted the rapid transition of the 3-in-1 NG solution into a stable hydrogel, confirming the efficacy of the gelation strategy (Fig. S3(a) in the ESM) [40]. TEM imaging revealed monodisperse spherical nanoparticles (Fig. 2(d)) while SEM of the *in situ*-formed hydrogel (Alg-PBA-Man/TPGS; APMT) showed a porous architecture composed of fascicled, needle-like aggregates forming a continuous network (Fig. 2(e)) — distinct from conventional Alg gels [35]. 3-in-1 NG exhibited an average particle size of 277.9 ± 4.4 nm with a narrow PDI of 0.17 ± 0.01 and a near-neutral zeta potential of −0.53 ± 0.05 mV (Fig. 2(f)). The improved uniformity of the dispersion, as indicated by the reduced PDI, correlated with the introduction of TPGS. The change in surface zeta potential of 3-in-1 NG is mainly attributed to ionic crosslinking between Fe^{2+} and Alg carboxyl groups [41], while the surface mannose residues further modulate the presentation of surface charge through steric shielding. Rheological analysis demonstrated a robust gel state ($G' > G''$) at shear stresses below 2450 Pa, transitioning to a sol state ($G' < G''$) at higher stresses (> 2832 Pa). The frequency-independent storage modulus (G') and time-dependent stability further confirmed the structural integrity of the hydrogel network (Fig. 2(g)).

The release behavior of mannose and TPGS demonstrated pH dependence. A markedly accelerated release was observed under acidic conditions, particularly at pH 5.5. As shown in Fig. 2(h), the cumulative release of mannose at 108 h reached 97.7% at pH 5.5 and 74.7% at pH 6.5, compared to 70.3% at pH 7.4. A similar trend of enhanced release in acidic environments was also noted for TPGS (Fig. 2(i)), which can be attributed to the protonation-induced contraction of Alg, hydrolysis of boronic ester bonds, and acidic cleavage of TPGS ester linkages. Notably, Fe^{2+} release was exclusively triggered at pH 5.5 (Fig. 2(j)), reflecting specificity for

the acidic conditions. The behavior stems from synergistic effects include weakened Fe^{2+}-Alg coordination, acid-labile boronate cleavage, and TPGS-mediated release modulation. Importantly, the nanogel retained structural integrity at physiological pH, preventing Fe^{2+} leakage and achieving 99.0% Fe^{2+} retention (Fig. 2(j) and Fig. S4(a) in the ESM). All formulations maintained excellent colloidal stability over 7 days at 4 °C, with negligible changes in size or surface potential (Figs. S4(b)–S4(d) in the ESM), highlighting their suitability for biomedical use. Together, these results demonstrate the successful design of a pH-responsive nanoplatform capable of targeted payload release in acidic regions while maintaining stability under physiological conditions.

3.2 *In vitro* anti-tumor activity of 3-in-1 NG

The anti-tumor efficacy of the 3-in-1 NG was systematically investigated using the 4T1 murine breast cancer cell line, a well-established TNBC model [42]. Cellular uptake studies confirmed the nanocarrier's superior delivery efficiency, with FITC-labeled 3-in-1 NG exhibiting time-dependent internalization and significantly higher intracellular accumulation compared to free Fe^{2+} (Figs. 3(a) and 3(b), and Table S2 in the ESM). The cytotoxicity profile further highlighted the combinatorial advantage of the nanogel, as the ternary formulation induced significantly stronger tumor cell killing than individual components or dual-combination nanogels (Figs. 3(c)–3(e)), while maintaining excellent biocompatibility with normal cells (> 95% viability, Fig. S5 in the ESM). Mechanistically, the 3-in-1 NG triggered robust apoptosis in 4T1 cells, achieving a 57.5% apoptotic rate—substantially higher than those induced by 2 NG-1 (23.7%) or 2 NG-2 (31.4%) (Fig. 3(f)). The potent effect was attributed to the synergistic interplay of mannose-mediated glycolysis disruption, TPGS-induced ICD, and Fe^{2+}-driven ferroptosis activation.

The acidic TME, characterized by elevated lactate levels (~ 40 mM), is a key driver of tumor aggressiveness and metastasis [43]. Under such conditions, 3-in-1 NG effectively neutralized lactate-induced pro-migratory effects, reducing cell migration by 80.1% and invasion capacity by 66.6% compared to the control (Fig. S6 in the ESM). While untreated cells exhibited accelerated wound healing in response to lactate, the nanogel maintained its strong anti-migratory activity even in acidic conditions. These results collectively demonstrate the multifaceted anti-tumor mechanisms of the 3-in-1 NG, which integrates enhanced drug delivery, synergistic cytotoxicity, and the induction of multiple cell death pathways (apoptosis, ferroptosis, and ICD), along with potent suppression of tumor cell motility-all critical features for countering the aggressive and metastatic nature of TNBC [44].

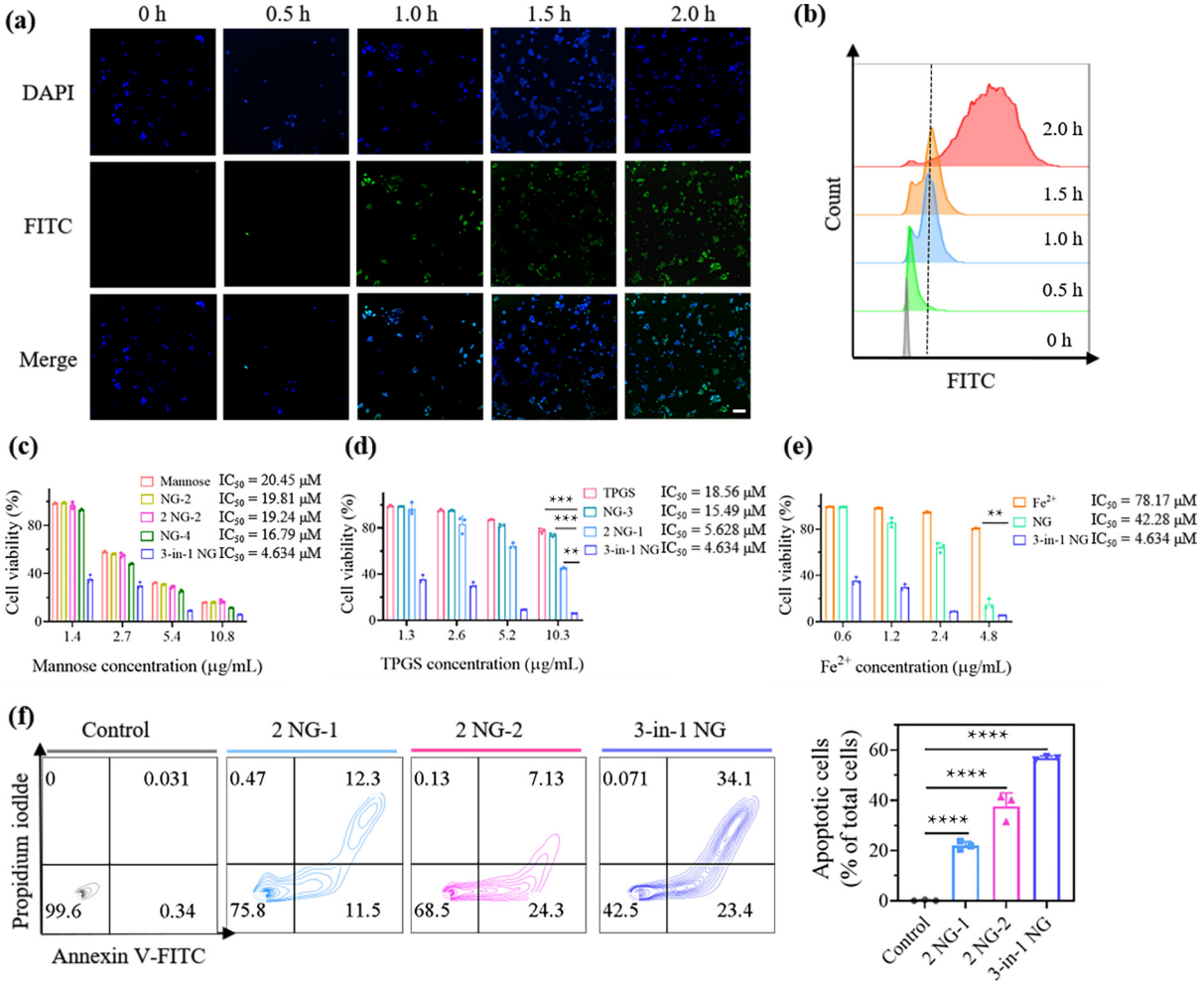

Figure 3 *In vitro* anti-tumor activity of 3-in-1 NG evaluated in 4T1 cells. (a) Time-dependent cellular uptake of FITC-labeled 3-in-1 NG (green) with 4′,6-diamidino-2-phenylindole (DAPI) nuclear staining (blue; scale bar: 50 μm) and (b) quantitative flow cytometry analysis of intracellular accumulation. Cytotoxicity profiling of (c) mannose, 2 NG-2, and 3-in-1 NG; (d) TPGS and 2 NG-1; and (e) Fe^{2+} and NG. (f) Apoptosis induction assessed by Annexin V-FITC/PI staining. Data are represented as mean ± SD ($n = 3$). $^{**}P < 0.01$, $^{***}P < 0.001$, $^{****}P < 0.0001$.

3.3 3-in-1 NG induces ferroptosis, glycolysis disruption, and ICD *in vitro*

3-in-1 NG exhibited a potent capacity to coordinately induce ferroptosis, disrupt glycolysis, and trigger ICD in 4T1 cells, with these mechanisms operating in a mutually reinforcing manner. Ferroptosis induction was evidenced by significantly elevated LPO and depleted antioxidant capacity (Figs. 4(a)–4(e)). The nanogel formulation markedly enhanced Fe^{2+}-mediated effects, with both NG and 3-in-1 NG showing superior LPO accumulation compared to free Fe^{2+} (Figs. 4(b)–4(d)). Within the 2 NG-2 formulation, the

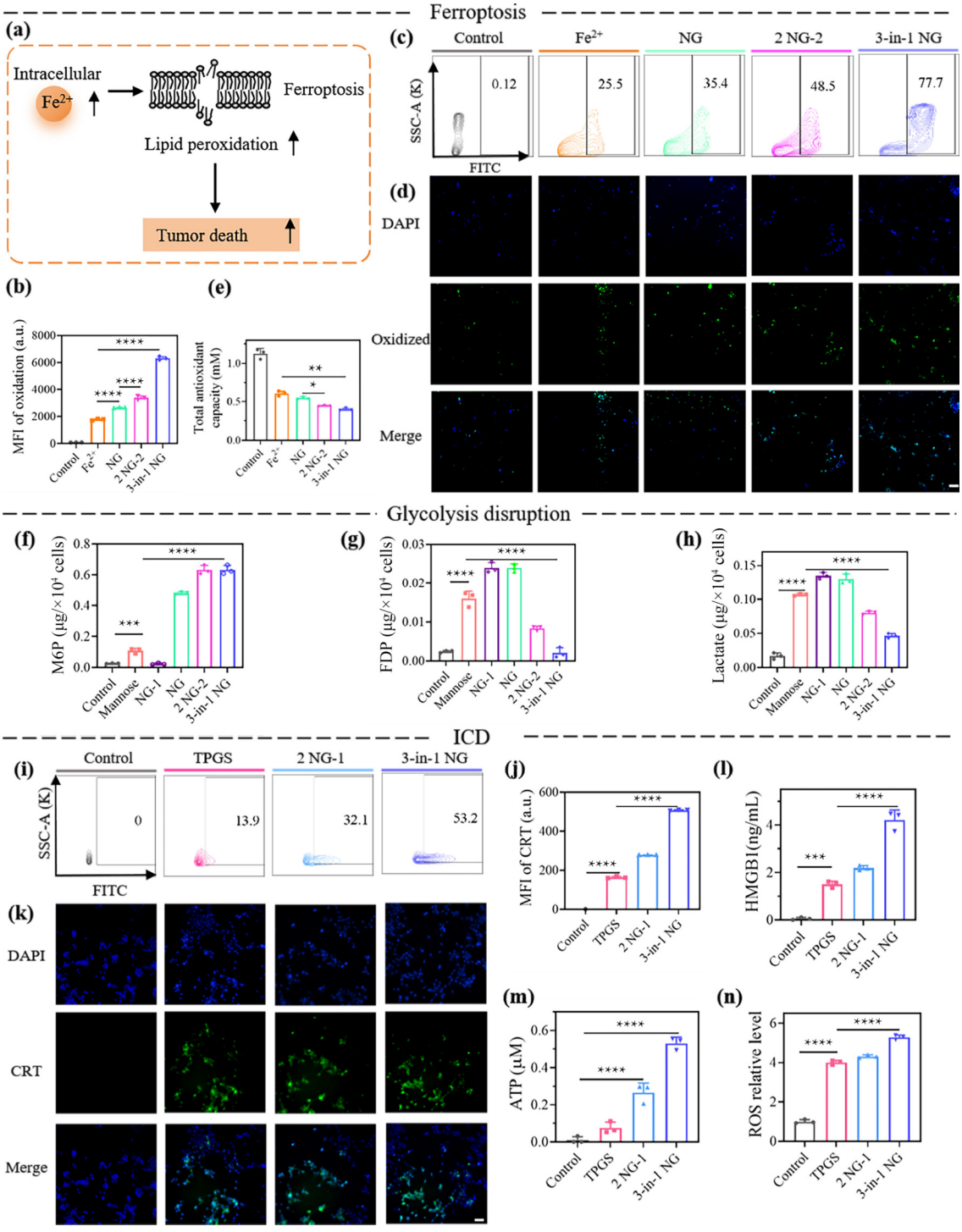

Figure 4 3-in-1 NG simultaneously triggers ferroptosis, glycolysis disruption, and ICD in 4T1 cells, as demonstrated by (a) the ferroptosis mechanism mediated by Fe^{2+} cross-linking in the nanogel, (c) flow cytometry and (b) quantification analysis of cellular oxidation status, (d) immunofluorescence visualization of LPO (green), and (e) measurement of total antioxidant capacity depletion. The nanogel's glycolysis interference is evidenced by (f) significant M6P accumulation, (g) FDP reduction, and (h) lactate depletion. ICD induction is shown through (i) flow cytometry analysis, (j) quantitative analysis, and (k) immunofluorescence analysis of CRT exposure exposure (scale bar: 50 μm), (l) HMGB1 release, and (m) ATP secretion, and (n) amplified ROS generation. Data are represented as mean ± SD (n = 3). $^{*}P < 0.05$, $^{**}P < 0.01$, $^{***}P < 0.001$, $^{****}P < 0.0001$.

mannose component contributed to effective glycolytic inhibition, thereby heightening cellular sensitivity to ferroptosis (Figs. 4(b)–4(d)). Notably, the mannose component contributed to the process by alleviating TME acidosis, thereby creating favorable conditions for sustained ferroptotic activity [45].

Glycolysis analysis further revealed the interconnected nature of these mechanisms. Compared to the mannose group, treatment with 3-in-1 NG resulted pronounced intracellular M6P accumulation (Fig. 4(f)), accompanied by depletion of critical glycolytic intermediates including FDP and lactate (Figs. 4(g) and 4(h)). The glycolytic blockade not only starved tumor cells of energy but also directly potentiated ferroptosis by reducing the lactate-mediated quenching of ROS [46]. The mechanism underlying M6P accumulation is ion-specific (Fig. 4(f)): Fe^{2+} within the NG acts as a pro-oxidant, generating ROS via Fenton reactions that induce oxidative cleavage of the Alg backbone. The resulting oligosaccharide fragments may enter core metabolic pathways, altering the hexose phosphate pool [47, 48]. Furthermore, Fe^{2+} serves as a crucial cofactor and signaling molecule, capable of reshaping glucose metabolic networks and indirectly influencing M6P dynamics [49]. In contrast, Ca^{2+} within the NG-1 lacks the redox activity and thus fails to induce significant metabolic perturbations. This highlights the critical influence of the crosslinking ion's intrinsic bioactivity on the nanogel's function and suggests that Fe^{2+}-driven metabolic effects synergize with mannose-mediated interference to promote profound metabolic reprogramming. Simultaneously, 3-in-1 NG triggered robust ICD markers. Surface CRT exposure (Figs. 4(i)–4(k)), HMGB1 release (Fig. 4(l)), and ATP secretion (Fig. 4(m)) were all significantly enhanced compared to single-component treatments.

The synergistic interaction among the components of 3-in-1 NG was particularly evident in the context of intracellular ROS generation. Compared to the TPGS-treated group, the combined action of Fe^{2+} and TPGS in 3-in-1 NG generated massive ROS amplification (Fig. 4(n)). The oxidative burst served dual purposes: fueling ferroptosis while simultaneously creating the oxidizing milieu necessary for optimal ICD induction [50–52]. Collectively, these findings illustrate a coordinated and mutually reinforcing mechanism of action, wherein glycolytic inhibition increases cellular susceptibility to ferroptosis, the ensuing ferroptotic process amplifies immunogenic signaling, and the activated immune response in turn exerts further metabolic pressure on tumor cells. The multi-directional interplay enables 3-in-1 NG to exert continuous and multi-faceted suppression of TNBC progression [53, 54].

3.4 3-in-1 NG inhibits tumor growth through synergistic therapy

The therapeutic efficacy of 3-in-1 NG was systematically evaluated in 4T1 tumor-bearing BALB/c mice, a clinically relevant model for TNBC (Fig. 5(a)) [55]. A stepwise series of control groups was employed to precisely deconvolute the contribution of each therapeutic module: a mannose-only group to isolate the effect of glycolysis disruption, 2 NG-1 to evaluate the combination of ferroptosis induction and ICD without active glycolysis disruption, and 2 NG-2 to examine the synergy between ferroptosis and metabolic inhibition in the absence of the ICD component. This design allowed for a definitive assessment of whether the complete 3-in-1 NG outperformed its dual-combination counterparts and to validate the essential role of integrating metabolic inhibition with the ferroptosis or ICD core for achieving optimal therapeutic outcomes.

Longitudinal monitoring via IVIS imaging, tumor growth curves, and quantitative inhibition rates consistently demonstrated potent tumor suppression (Figs. 5(b)–Figs. 5(d)). This robust anti-tumor activity originated from a mutually reinforcing interplay among the three therapeutic modalities: mannose-mediated glycolysis inhibition depleted cellular energy reserves and alleviated tumor acidosis, thereby enhancing the susceptibility of cancer cells to Fe^{2+}-driven ferroptosis [21]. The process was further potentiated by TPGS-induced ICD, which promoted the exposure of DAMPs. The metabolic disruption and ferroptosis jointly contributed to the release of LPO products and ICD-related signals such as CRT, HMGB1, and ATP. These molecules in turn facilitated the recruitment and activation of immune cells, whose cytokine secretion and cytotoxic functions further aggravated metabolic stress in the TME [24, 56, 57]. The *in situ*-gelling nanogel architecture played a pivotal role in maintaining this coordinated action, as its sustained retention within the tumor ensured continuous localized delivery of all three active components while minimizing systemic exposure [58].

Histopathological examination revealed extensive tumor destruction (H&E staining) and apoptosis (TUNEL) specifically in 3-in-1 NG-treated groups (Figs. 5(e) and 5(f)), underscoring the successful translation of *in vitro* mechanisms to tissue-level efficacy. Notably, the potent anti-tumor activity was achieved systemic toxicity, as evidenced by preserved organ histology, steady body weight gain, and normal behavioral indicators (Fig. S7 in the ESM). Further evaluation of iron homeostasis revealed no significant alterations in serum ferritin or total iron concentration (Figs. 5(g) and 5(h)), confirming that the nanogel treatment did not disrupt systemic iron balance and underscoring its high biocompatibility [59, 60].

Together, these results illustrate how 3-in-1 NG establishes a self-amplifying therapeutic cascade in which glycolysis inhibition sensitizes tumors to ferroptosis, ferroptotic debris and ICD signals activate immune responses, and immune effector functions in turn sustain metabolic suppression [21]. The coordinated multi-mechanism interaction represents a paradigm shift from conventional combination therapies, generating interdependent anti-tumor effects that evolve dynamically within the TME, thereby offering a promising strategy for TNBC treatment.

3.5 3-in-1 NG remodels the tumor immune microenvironment

The immunomodulatory capacity of 3-in-1 NG was systematically validated through flow cytometric analysis of the 4T1 tumor model, revealing a coordinated cascade of immune activation events (Fig. S8 in the ESM). Treatment with 3-in-1 NG triggered robust DC maturation, evidenced by significant upregulation of CD80/CD86 co-stimulatory molecules in both lymph nodes (Fig. 6(a)) and tumor tissues (Fig. 6(b)), establishing the foundation for effective antigen presentation and T cell priming. The DC activation translated into substantial recruitment of tumor-infiltrating lymphocytes, with dramatic increases in both cytotoxic $CD8^+$ T cells (Fig. 6(c)) and helper $CD4^+$ T cells (Fig. 6(d)), effectively converting the immunologically inert TNBC microenvironment into a T cell-inflamed phenotype.

The immunomodulatory influence of the nanogel extended

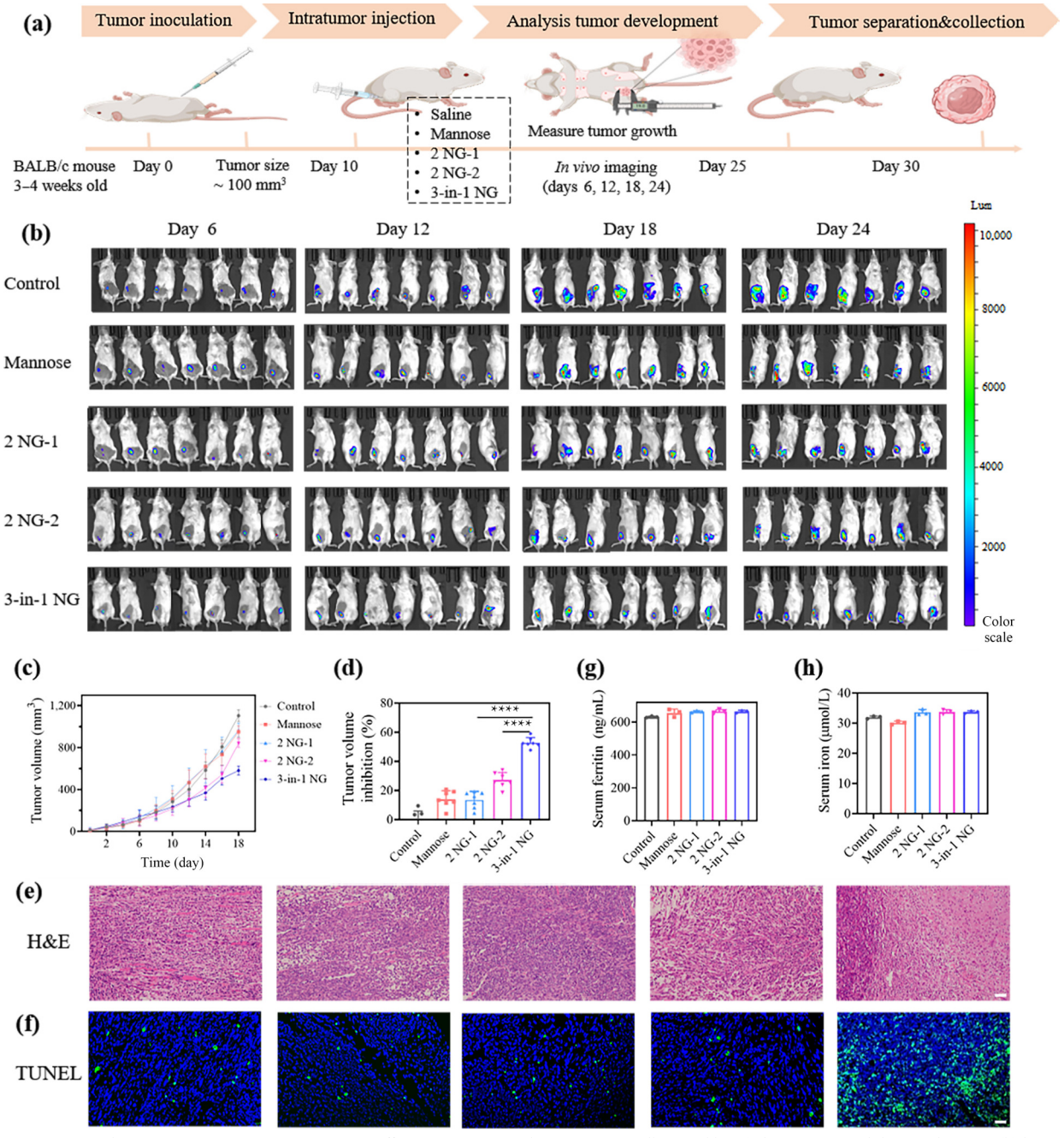

Figure 5 3-in-1 NG demonstrates potent *in vivo* anti-tumor efficacy in 4T1 tumor-bearing mice, as illustrated by (a) the experimental design schematic, (b) longitudinal bioluminescence imaging showing tumor suppression, and (c) tumor growth curves with corresponding (d) quantitative analysis of tumor volume inhibition. (e) H&E-stained tumor sections (scale bar: 2 mm) and (f) TUNEL apoptosis assays (scale bar: 50 μm) provide histological evidence of tumor destruction and extensive cell death. Systemic iron metabolism is assessed via serum levels of (g) ferritin and (h) iron. Data are represented as mean ± SD ($n = 7$). $^{****}P < 0.0001$.

beyond adaptive immunity to reshape innate immune components, particularly through metabolic reprogramming of tumor-associated macrophages (TAMs). The mannose component selectively targeted MR-expressing M2 macrophages while TPGS-mediated ICD alleviated lactate-mediated immunosuppression, collectively driving a pronounced M2-to-M1 phenotypic shift (Fig. 6(e)) [15, 61]. The repolarization process was mechanistically supported by the activation of key signaling pathways, including enhanced phosphorylation of NF-κB p65 and STAT1 (Fig. S9 in the ESM), both established regulators of M1 macrophage polarization. Furthermore, 3-in-1 NG induced a profound reshaping of the cytokine landscape, significantly elevating pro-inflammatory TNF-α (Fig. 6(f)) and IFN-γ (Fig. 6(g)), and IL-6 (Fig. 6(h)), while suppressing immunosuppressive TGF-β (Fig. 6(i)).

Critically, the immunomodulatory, metabolic, and ferroptotic activities of 3-in-1 NG function in a mutually reinforcing manner. ICD-generated tumor antigens enhanced DC activation and T cell responses, while T cell-derived IFN-γ further sensitized tumor cells to ferroptosis. Simultaneously, the metabolic disruption of glycolysis depleted immunosuppressive metabolites, and ferroptosis generated lipid peroxides acted as danger signals to sustain immune activation [21, 62]. The tripartite

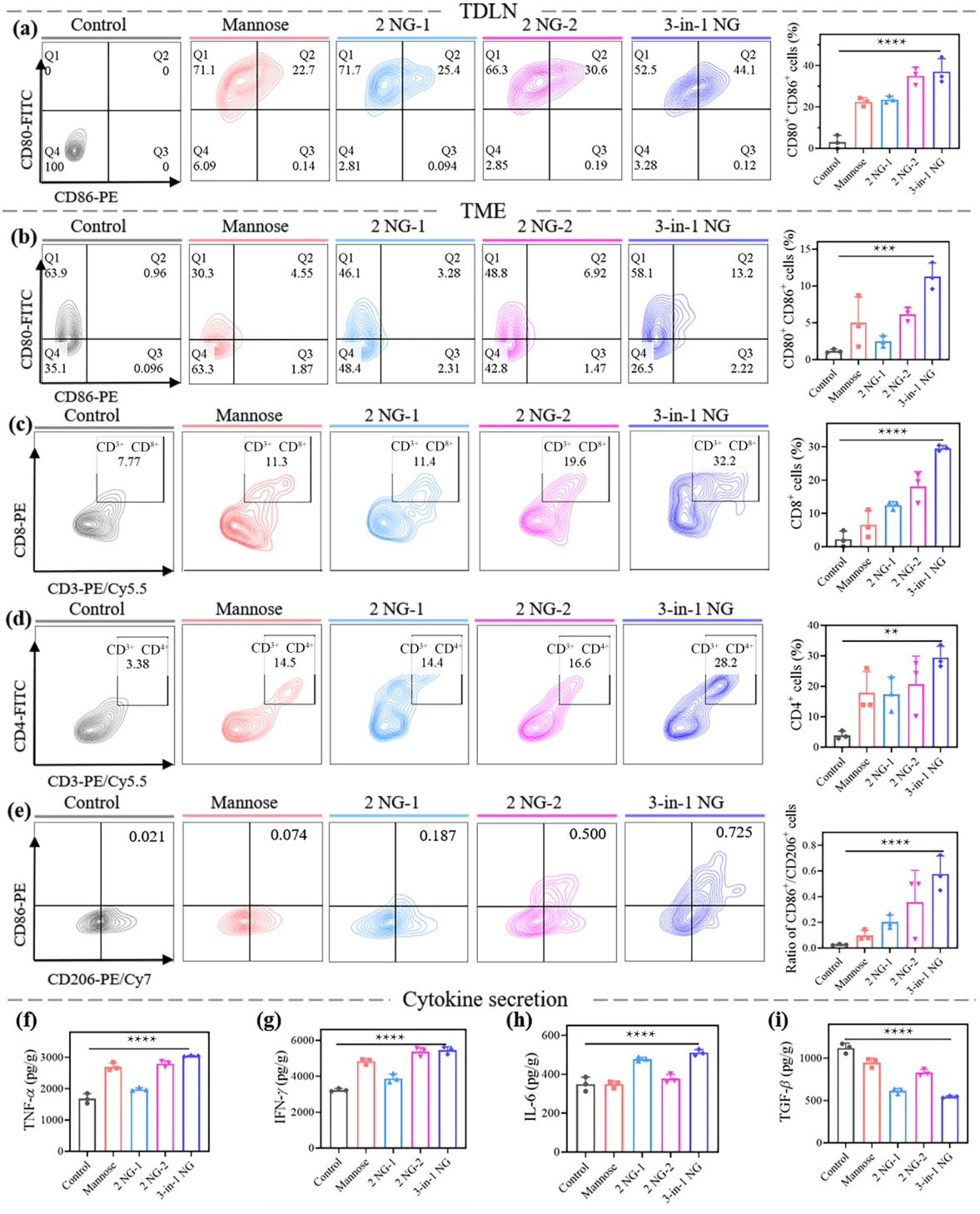

Figure 6 3-in-1 NG induces comprehensive immunomodulation within the TME, as demonstrated by upregulated DC activation markers (CD80/CD86) in both (a) TDLN and (b) tumor tissues, enhanced infiltration of (c) cytotoxic $CD8^+$ and (d) helper $CD4^+$ T cells, (e) shifted macrophage polarization toward the pro-inflammatory M1 phenotype, and significantly altered cytokine profiles featuring elevated (f) TNF-α, (g) IFN-γ, and (h) IL-6 alongside suppressed (i) TGF-β expression, collectively indicating successful TME reprogramming from immunosuppressive to immunostimulatory. Data are represented as mean ± SD (n = 3). $^*P < 0.01$, $^{***}P < 0.001$, $^{****}P < 0.0001$.

synergy-metabolic reprogramming enabling immune activation which in turn potentiates ferroptosis-represents a breakthrough approach for overcoming TNBC's immunosuppressive barriers, demonstrating how 3-in-1 NG's components work in concert to establish a continuously evolving anti-tumor ecosystem within the TME [58].

3.6 3-in-1 NG synergistically regulates ferroptosis, glycolysis inhibition and immune activation

3-in-1 NG establishes a mutually reinforcing therapeutic mechanism in 4T1 tumors, where ferroptosis induction, glycolysis disruption, and ICD reciprocally amplify each other's anti-tumor

effects [21, 62]. Through its co-delivery to the tumor and acid microenvironment-responsive release, the nanogel achieves intratumoral total iron ion levels and depleting antioxidant capacity (Figs. 7(a)–7(c)), establishing an iron-rich oxidative conditions for LPO. The ferroptotic cascade is metabolically augmented by the nanogel's dual impact on glycolysis-significant M6P accumulation coupled with depletion of FDP and lactate (Figs. 7(d)–7(f)) — which not only starves tumors of energy but also alleviates TME acidosis to further potentiate iron-mediated oxidative stress [21].

The immunogenic component further amplifies the therapeutic outcome, as evidenced by robust CRT exposure and HMGB1 release (Figs. 7(g)–7(i)) that transform the tumor into an immunogenic niche. Molecular profiling reveals how this tri-modal attack overcomes therapeutic challenges: GPX4 downregulation and ACSL4 upregulation (Figs. 7(j)–7(l)) create a lipid landscape superior ferroptosis induction by simultaneously elevating vulnerable to peroxidation, while coordinated reduction of MCL-1 and BCL-XL (Figs. 7(j), 7(m), and 7(n)) dismantles apoptotic defenses [63]. Crucially, these mechanisms operate in an integrated

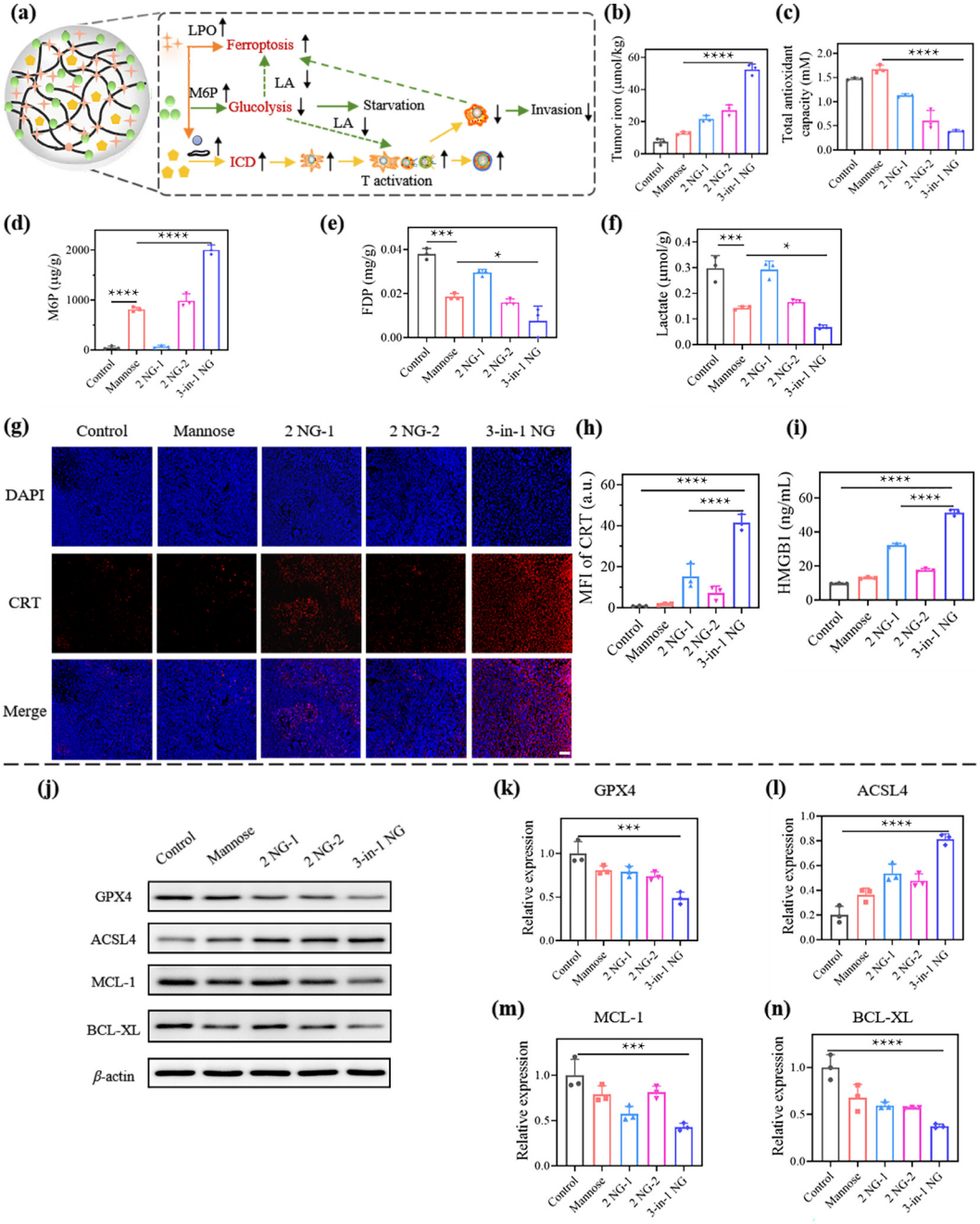

Figure 7 (a) Schematic illustration of the synergistic antitumor mechanism mediated by 3-in-1 NG, which integrates ferroptosis induction, glycolysis inhibition, and ICD. 3-in-1 NG exerts coordinated therapeutic actions in 4T1 tumors, as demonstrated by (b) increased intratumoral total iron ion levels and (c) decreased antioxidant capacity, confirming ferroptosis; impaired glycolysis supported by (d) accumulation of M6P, (e) reduction in FDP, and (f) depletion of lactate; and induction of ICD evidenced by (g) enhanced CRT exposure (red fluorescence; scale bar: 100 μm), (h) corresponding quantitative analysis of CRT, and (i) HMGB1 release. (j) Western blot analysis of protein expression related to ferroptosis: (k) GPX4 and (l) ACSL4, and apoptosis: (m) MCL-1 and (n) BCL-XL. Data are represented as mean ± SD (n = 3). *P < 0.05, ***P < 0.001, ****P < 0.0001

and mutually reinforcing manner. Glycolysis inhibition depletes antioxidant reserves and sensitizes cells to ferroptosis; ferroptosis-derived signals and ICD-associated DAMPs recruit and activate immune effectors. Subsequently, immune-derived cytokines, such as IFN-γ and TNF-α, further perturb tumor metabolism and exacerbate oxidative stress, creating a self-propagating anti-tumor response [22]. The coordinated strategy effectively addresses TNBC's treatment challenges by concurrently exploiting its metabolic addiction, redox vulnerabilities, and immune evasion tactics, representing a paradigm shift from conventional combination therapies through its ability to create an evolving anti-tumor ecosystem within the TME [62].

4 Conclusions

This study presents an innovative 3-in-1 nanogel system that overcomes TNBC treatment challenges through a self-sustaining therapeutic cycle combining glycolysis disruption, ferroptosis induction, and immune activation [21, 24, 62]. Unlike conventional chemotherapy or biologics, the 3-in-1 NG achieves exceptional therapeutic efficacy while maintaining superior biocompatibility [14, 25, 64]. 3-in-1 NG's therapeutic advantage stems from its ability to initiate a synergistic cascade: mannose-mediated glycolysis inhibition depletes antioxidant reserves to sensitize tumors to Fe^{2+}-driven ferroptosis, while TPGS-induced ICD recruits immune effectors that further amplify metabolic disruption through cytokine signaling, thereby exerting continuous multi-faceted pressure on tumor survival pathways [21, 62]. These mutually reinforcing mechanisms represent a paradigm shift in cancer therapy, demonstrating how precisely engineered natural polymers can simultaneously exploit metabolic addiction, redox homeostasis, and immune evasion-three hallmarks of treatment-refractory cancers [65]. Beyond TNBC, the platform's modular design offers broad applicability for glycolytic tumors like pancreatic and hepatocellular carcinomas, with potential for customization through alternative sugar modifications, therapeutic ion combinations, or integration with immune checkpoint inhibitors. By transforming conventional combination therapy into a dynamically evolving therapeutic ecosystem, this research opens new possibilities for next-generation nanomedicine approaches to combat aggressive malignancies.

Electronic Supplementary Material: Supplementary material (characterization of materials (FT-IR spectra, Alg M/G ratio), physicochemical properties of the nanogels (size, PDI, gelation behavior, stability), analytical calibration curves (PBA, mannose, TPGS, Fe^{2+}), Fe^{2+} retention assays, biological data (intracellular Fe^{2+}, cytotoxicity on L929 cells, anti-metastatic effects on 4T1 cells), *in vivo* safety (body weight, H&E staining of major organs), flow cytometry gating strategy, and further mechanism studies on macrophage repolarization via STAT1/NF-κB pathways) is available in the online version of this article at https://doi.org/10.26599/NR.2026.94908349.

Data availability

All data needed to support the conclusions in the paper are presented in the manuscript and/or the Electronic Supplementary Material. Additional data related to this paper may be requested from the corresponding author upon request.

Acknowledgements

This work is granted by the National Key Research and Development Program of China (No. 2022YFC3501905) and PhD Scientific Research and Innovation Foundation of Sanya Yazhou Bay Science and Technology City (No. HSPHDSRF-2023-01-013).

Declaration of competing interest

All the contributing authors report no conflict of interests in this work.

Author contribution statement

B. X. S., S. R. G., and C. M. Z. conceived the idea. B. X. S. fabricated the samples, conducted experiments and wrote the manuscript. Y. M. Q., H. C. Z., Z. Z. W., and C. F. W. joined the experiments. Y. M. Q., Y. P. T., Y. Y. X., Z. J., F. H. W., and D. R. C. joined the discussions and gave useful suggestions. S. R. G. supervised the project. All the authors have approved the final manuscript.

Informed consent

Not applicable.

Ethics statement

The animal experiments were carried out following the guidelines of the Shanghai Jiao Tong University Institutional Committee for the Care and Use of Laboratory Animals and were approved by the Committee on Ethical Use of Animals of Shanghai Jiao Tong University (Ethical code: 2024-01-LY-CDR-111).

Use of AI statement

None.

References

[1] Kong, L. R.; Gupta, K.; Wu, A. J.; Perera, D.; Ivanyi-Nagy, R.; Ahmed, S. M.; Tan, T. Z.; Tan, S. L. W.; Fuddin, A.; Sundaramoorthy, E. et al. A glycolytic metabolite bypasses "two-hit" tumor suppression by BRCA2. *Cell* **2024**, *187*, 2269–2287.e16.

[2] Feng, Y. L.; Wang, J. L.; Ning, X.; Li, A. Y.; You, Q.; Su, W. Z.; Wang, D. P.; Shi, J. Y.; Zhou, L.; Cao, F. F. et al. $BaTiO_3$@Au nanoheterostructure suppresses triple-negative breast cancer by persistently disrupting mitochondrial energy metabolism. *Nano Res.* **2023**, *16*, 2775–2785.

[3] Anemone, A.; Consolino, L.; Conti, L.; Irrera, P.; Hsu, M. Y.; Villano, D.; Dastrù, W.; Porporato, P. E.; Cavallo, F.; Longo, D. L. Tumour acidosis evaluated *in vivo* by MRI-CEST pH imaging reveals breast cancer metastatic potential. *Br. J. Cancer* **2021**, *124*, 207–216.

[4] Gonzalez, P. S.; O'Prey, J.; Cardaci, S.; Barthet, V. J. A.; Sakamaki, J. I.; Beaumatin, F.; Roseweir, A.; Gay, D. M.; Mackay, G.; Malviya, G. et al. Mannose impairs tumour growth and enhances chemotherapy. *Nature* **2018**, *563*, 719–723.

[5] Selcuk, S. Y.; Yang, X. L.; Bai, B. J.; Zhang, Y. J.; Li, Y. Z.; Aydin, M.; Unal, A. F.; Gomatam, A.; Guo, Z.; Angus, D. M. et al. Automated HER2 scoring in breast cancer images using deep learning and pyramid sampling. *BME Front.* **2024**, *5*, 0048.

[6] Liu, Y. C.; Sun, Q. Y.; Guo, J. W.; Yan, L.; Yan, Y.; Gong, Y. T.; Lin, J. Y.; Yuan, H.; Jin, J. M.; Wang, B. et al. Dual ferroptosis induction in N2-TANs and TNBC cells via FTH1 targeting: A therapeutic strategy for triple-negative breast cancer. *Cell Rep. Med.* **2025**, *6*, 101915.

[7] Liu, Y. H.; Wu, H.; Wang, S. Q.; Zhang, X. T.; Gong, L. M.; Xiao, C. C.; Liu, C. F.; Chen, L. Q.; Zhao, H. M.; Liu, C. et al. Biomimetic multifunctional nanodrugs enable regulating abnormal tumor metabolism and amplifying PDT-induced immunotherapy for synergistically enhanced tumor ablation. *Mater. Today* **2023**, *68*, 125–147.

[8] Won, K. A.; Spruck, C. Triple‐negative breast cancer therapy: Current and future perspectives (Review). *Int. J. Oncol* **2020**, *57*, 1245–1261.

[9] Wei, Z. W.; Huang, L. F.; Cui, L.; Zhu, X. Mannose: Good player and assister in pharmacotherapy. *Biomed. Pharmacother.* **2020**, *129*, 110420.

[10] Dong, Z. L.; Jiao, X.; Wang, Z. G.; Yuan, K.; Yang, Y. Q.; Wang, Y.; Li, Y. T.; Wang, T. C.; Kan, T. Y.; Wang, J. et al. D-mannose alleviates intervertebral disc degeneration through glutamine metabolism. *Mil. Med. Res.* **2024**, *11*, 28.

[11] Jin, H. Y.; Liu, X.; Liu, H. X. Biological function, regulatory mechanism, and clinical application of mannose in cancer. *Biochim. Biophys. Acta Rev. Cancer* **2023**, *1878*, 188970.

[12] Hou, L.; Gong, X.; Yang, J.; Zhang, H. J.; Yang, W. J.; Chen, X. Y. Hybrid-membrane-decorated Prussian blue for effective cancer immunotherapy via tumor-associated macrophages polarization and hypoxia relief. *Adv. Mater.* **2022**, *34*, 2200389.

[13] Ren, X. J.; Cheng, Z.; He, J. M.; Yao, X. M.; Liu, Y. Q.; Cai, K. Y.; Li, M. H.; Hu, Y.; Luo, Z. Inhibition of glycolysis-driven immunosuppression with a nano-assembly enhances response to immune checkpoint blockade therapy in triple negative breast cancer. *Nat. Commun.* **2023**, *14*, 7021.

[14] Dhanalakshmi, M.; Sruthi, D.; Jinuraj, K. R.; Das, K.; Dave, S.; Andal, N. M.; Das, J. Mannose: A potential saccharide candidate in disease management. *Med. Chem. Res.* **2023**, *32*, 391–408.

[15] Zou, C. M.; Tang, Y. P.; Zeng, P.; Cui, D. R.; Amili, M. A.; Chang, Y.; Jin, Z.; Shen, Y. Y.; Tan, S. W.; Guo, S. R. cRGD-modified nanoparticles of multi-bioactive agent conjugate with pH-sensitive linkers and PD-L1 antagonist for integrative collaborative treatment of breast cancer. *Nanoscale Horiz.* **2023**, *8*, 870–886.

[16] Wei, P. H.; Niu, X. G.; Wang, D. L.; Du, C. Z.; Zhu, M. T.; Zheng, H. J.; Hu, Y. R.; Tian, Y.; Huang, W.; Ding, C. Y. et al. A glutathione-responsive ferroptotic inducer with elevated labile iron pool and self-supplied peroxide for chemodynamic therapy. *Mater. Today Bio.* **2025**, *32*, 101913.

[17] Ye, Z. R. J.; Xie, B.; Tao, Y. G.; Xiao, D. S. Mechanism of ferroptosis and its role in disease development. *Int. J. Biol. Sci.* **2025**, *21*, 5328–5360.

[18] Ye, L.; Wen, X. Q.; Qin, J. L.; Zhang, X.; Wang, Y. P.; Wang, Z. Y.; Zhou, T.; Di, Y. Q.; He, W. L. Metabolism-regulated ferroptosis in cancer progression and therapy. *Cell Death Dis.* **2024**, *15*, 196.

[19] Zhou, Q. Z.; Yu, L. X.; Cook, J. R.; Qiang, L.; Sun, L. Deciphering the decline of metabolic elasticity in aging and obesity. *Cell Metab.* **2023**, *35*, 1661–1671.e6.

[20] Qiu, Y. J.; Su, Y. P.; Xie, E. M.; Cheng, H. C.; Du, J.; Xu, Y.; Pan, X. L.; Wang, Z.; Chen, D. G.; Zhu, H. et al. Mannose metabolism reshapes T cell differentiation to enhance anti-tumor immunity. *Cancer Cell* **2025**, *43*, 103–121.e8.

[21] Tang, Q. Q.; Wang, Y. Y.; Yan, B.; Zhang, J.; Wang, T.; Fang, Y.; Ye, Z. R.; Zhang, N.; Zhang, N. N.; Wu, Z. et al. Intracellular magnetic hyperthermia sensitizes sorafenib to orthotopic hepatocellular carcinoma via amplified ferroptosis. *ACS Nano* **2024**, *18*, 29804–29819.

[22] Jiang, J.; Yan, Y.; Yang, C. H.; Cai, H. Immunogenic cell death and metabolic reprogramming in cancer: Mechanisms, synergies, and innovative therapeutic strategies. *Biomedicines* **2025**, *13*, 950.

[23] Yang, Z.; Su, W.; Wei, X. Y.; Qu, S.; Zhao, D.; Zhou, J. W.; Wang, Y. J.; Guan, Q.; Qin, C.; Xiang, J. et al. HIF-1α drives resistance to ferroptosis in solid tumors by promoting lactate production and activating SLC1A1. *Cell Rep.* **2023**, *42*, 112945.

[24] Pawłowska, M.; Nuszkiewicz, J.; Jarek, D. J.; Woźniak, A. Ferroptosis and Metabolic Dysregulation: Emerging Chemical Targets in Cancer and Infection. *Molecules* **2025**, *30*, 3020.

[25] Baldi, A.; Braat, S.; Hasan, M. I.; Bennett, C.; Barrios, M.; Jones, N.; Abdul Azeez, I.; Wilcox, S.; Roy, P. K.; Bhuiyan, M. S. A. et al. Effects of iron supplements and iron-containing micronutrient powders on the gut microbiome in Bangladeshi infants: A randomized controlled trial. *Nat. Commun.* **2024**, *15*, 8640.

[26] Yang, C. L.; Wu, T. T.; Qi, Y.; Zhang, Z. P. Recent advances in the application of vitamin E TPGS for drug delivery. *Theranostics* **2018**, *8*, 464–485.

[27] Xie, P.; Yang, S. T.; Huang, Y. F.; Zeng, C.; Xin, Q.; Zeng, G. F.; Yang, S. N.; Xia, P. F.; Tang, X. H.; Tang, K. X. Carbon nanoparticles-Fe(II) complex for efficient tumor inhibition with low toxicity by amplifying oxidative stress. *ACS Appl. Mater. Interfaces* **2020**, *12*, 29094–29102.

[28] Mackie, W. Semi-quantitative estimation of the composition of alginates by infra-red spectroscopy. *Carbohydr. Res.* **1971**, *20*, 413–415.

[29] Liu, S.; Zhao, Y. S.; Li, M.; Nie, L.; Wei, Q. Q.; Okoro, O. V.; Jafari, H.; Wang, S. Y.; Deng, J.; Chen, J. H. et al. Bioactive wound dressing based on decellularized tendon and GelMA with incorporation of PDA-loaded asiaticoside nanoparticles for scarless wound healing. *Chem. Eng. J.* **2023**, *466*, 143016.

[30] Chu, C. K.; Joseph, A. J.; Limjoco, M. D.; Yang, J. W.; Bose, S.; Thapa, L. S.; Langer, R.; Anderson, D. G. Chemical tuning of fibers drawn from extensible hyaluronic acid networks. *J. Am. Chem. Soc.* **2020**, *142*, 19715–19721.

[31] Bazban-Shotorbani, S.; Dashtimoghadam, E.; Karkhaneh, A.; Hasani-Sadrabadi, M. M.; Jacob, K. I. Microfluidic directed synthesis of alginate nanogels with tunable pore size for efficient protein delivery. *Langmuir* **2016**, *32*, 4996–5003.

[32] Su, M.; Zhu, Y. Q.; Chen, J. B.; Zhang, B. B.; Sun, C. Y.; Chen, M. W.; Yang, X. Z. Microfluidic synthesis of manganese-alginate nanogels with self-supplying H_2O_2 capability for synergistic chemo/chemodynamic therapy and boosting anticancer immunity. *Chem. Eng. J.* **2022**, *435*, 134926.

[33] Mahmoudi, Z.; Mohammadnejad, J.; Razavi Bazaz, S.; Abouei Mehrizi, A.; Saidijam, M.; Dinarvand, R.; Ebrahimi Warkiani, M.; Soleimani, M. Promoted chondrogenesis of hMCSs with controlled release of TGF-β3 via microfluidics synthesized alginate nanogels. *Carbohydr. Polym.* **2020**, *229*, 115551.

[34] Tesfaldet, Z. O.; Van Staden, J. F.; Stefan, R. I. Sequential injection spectrophotometric determination of iron as Fe(II) in multi-vitamin preparations using 1, 10-phenanthroline as complexing agent. *Talanta* **2004**, *64*, 1189–1195.

[35] Monteiro, A. F.; Miguez, I. S.; Silva, J. P. R. B.; Da Silva, A. S. High concentration and yield production of mannose from açaí (*Euterpe oleracea* Mart.) seeds via mannanase-catalyzed hydrolysis. *Sci. Rep.* **2019**, *9*, 10939.

[36] Jin, X.; Tang, J. R.; Qiu, X. Y.; Nie, X. Y.; Ou, S. M.; Wu, G. Y.; Zhang, R. X.; Zhu, J. R. Ferroptosis: Emerging mechanisms, biological function, and therapeutic potential in cancer and inflammation. *Cell Death Discov.* **2024**, *10*, 45.

[37] Zhang, C. S.; Hawley, S. A.; Zong, Y.; Li, M. Q.; Wang, Z. C.; Gray, A.; Ma, T.; Cui, J. W.; Feng, J. W.; Zhu, M. J. et al. Fructose-1, 6-bisphosphate and aldolase mediate glucose sensing by AMPK. *Nature* **2017**, *548*, 112–116.

[38] Walenta, S.; Schroeder, T.; Mueller-Klieser, W. Lactate in solid malignant tumors: Potential basis of a metabolic classification in clinical oncology. *Curr. Med. Chem.* **2004**, *11*, 2195–2204.

[39] Song, R. J.; Wang, X. Y.; Johnson, M.; Milne, C.; Lesniak-Podsiadlo, A.; Li, Y. H.; Lyu, J.; Li, Z. S.; Zhao, C. Y.; Yang, L. Z. et al. Enhanced strength for double network hydrogel adhesive through cohesion-adhesion balance. *Adv. Funct. Mater.* **2024**, *34*, 2313322.

[40] Liu, C.; Li, M.; Dong, Z. X.; Jiang, D.; Li, X. J.; Lin, S. B.; Chen, D. M.; Zou, X. N.; Zhang, X. D.; Luker, G. D. Heterogeneous

microenvironmental stiffness regulates pro-metastatic functions of breast cancer cells. *Acta Biomater.* **2021**, *131*, 326–340.
[41] Zhang, Y. X.; Wang, Y. S.; Chen, Y.; Luan, Q. Y.; Ding, M. Y.; Chen, H. H. Effects of secondary cross-linking on the physicochemical properties of sodium alginate-hydrogel and *in vitro* release of anthocyanins. *Int. J. Biol. Macromol.* **2024**, *276*, 133926.
[42] Baklaushev, V. P.; Kilpeläinen, A.; Petkov, S.; Abakumov, M. A.; Grinenko, N. F.; Yusubalieva, G. M.; Latanova, A. A.; Gubskiy, I. L.; Zabozlaev, F. G.; Starodubova, E. S. et al. Luciferase expression allows bioluminescence imaging but imposes limitations on the Orthotopic mouse (4T1) model of breast cancer. *Sci. Rep.* **2017**, *7*, 7715.
[43] Zhang, Y.; Peng, Q.; Zheng, J. H.; Yang, Y. Z.; Zhang, X. M.; Ma, A. Y.; Qin, Y. X.; Qin, Z. L.; Zheng, X. The function and mechanism of lactate and lactylation in tumor metabolism and microenvironment. *Genes Dis.* **2023**, *10*, 2029–2037.
[44] Bianchini, G.; De Angelis, C.; Licata, L.; Gianni, L. Treatment landscape of triple-negative breast cancer - expanded options, evolving needs. *Nat. Rev. Clin. Oncol.* **2022**, *19*, 91–113.
[45] Zhang, R. N.; Yang, Y. J.; Dong, W. J.; Lin, M. G.; He, J.; Zhang, X. C.; Tian, T. G.; Yang, Y. L.; Chen, K.; Lei, Q. Y. et al. D-mannose facilitates immunotherapy and radiotherapy of triple-negative breast cancer via degradation of PD-L1. *Proc. Natl. Acad. Sci. USA* **2022**, *119*, e2114851119.
[46] Ždralević, M.; Vučetić, M.; Daher, B.; Marchiq, I.; Parks, S. K.; Pouysségur, J. Disrupting the 'Warburg effect' re-routes cancer cells to OXPHOS offering a vulnerability point via 'ferroptosis'-induced cell death. *Adv. Biol. Regul.* **2018**, *68*, 55–63.
[47] Alves, F.; Lane, D.; Nguyen, T. P. M.; Bush, A. I.; Ayton, S. In defence of ferroptosis. *Signal Transduct. Target. Ther.* **2025**, *10*, 2.
[48] Loveikyte, R.; Bourgonje, A. R.; Van Goor, H.; Dijkstra, G.; Van Der Meulen - De Jong, A. E. The effect of iron therapy on oxidative stress and intestinal microbiota in inflammatory bowel diseases: A review on the conundrum. *Redox Biol.* **2023**, *68*, 102950.
[49] Peters, K.; Staehlke, S.; Rebl, H.; Jonitz-Heincke, A.; Hahn, O. Impact of metal ions on cellular functions: A focus on mesenchymal stem/stromal cell differentiation. *Int. J. Mol. Sci.* **2024**, *25*, 10127.
[50] An, X. Q.; Yu, W. F.; Liu, J. B.; Tang, D. L.; Yang, L.; Chen, X. Oxidative cell death in cancer: Mechanisms and therapeutic opportunities. *Cell Death Dis.* **2024**, *15*, 556.
[51] Zhang, J.; Wei, Y. H.; Yue, Y. B.; Jiao, H. K.; Wu, Y.; Fu, W.; Lin, K. M.; Lu, C.; Mou, S.; Zhong, Q. RIPK4 promotes oxidative stress and ferroptotic death through the downregulation of ACSM1. *Proc. Natl. Acad. Sci. USA* **2024**, *121*, e2410628121.
[52] Cañeque, T.; Baron, L.; Müller, S.; Carmona, A.; Colombeau, L.; Versini, A.; Solier, S.; Gaillet, C.; Sindikubwabo, F.; Sampaio, J. L. et al. Activation of lysosomal iron triggers ferroptosis in cancer. *Nature* **2025**, *642*, 492–500.
[53] Munkácsy, G.; Santarpia, L.; Győrffy, B. Therapeutic potential of tumor metabolic reprogramming in triple-negative breast cancer. *Int. J. Mol. Sci.* **2023**, *24*, 6945.
[54] Zhang, Y.; Du, X. Y.; He, Z. J.; Gao, S.; Ye, L.; Ji, J. B.; Yang, X. Y.; Zhai, G. X. A vanadium-based nanoplatform synergizing ferroptotic-like therapy with glucose metabolism intervention for enhanced cancer cell death and antitumor immunity. *ACS Nano* **2023**, *17*, 11537–11556.
[55] Albores-Mendez, E. M.; Casanas-Pimentel, R. G.; Reyes-Chacon, I. R.; Cubas, J. M.; Lopez-Cruz, J.; Rincon-Huerta, J. A.; Camacho-Ibarra, A.; Martin-Martinez, E. S. Cancer progression is not different in mice of different gender inoculated with cells of the triple-negative 4T1 breast cancer model. *World J. Oncol.* **2022**, *13*, 249–258.
[56] Wiernicki, B.; Maschalidi, S.; Pinney, J.; Adjemian, S.; Vanden Berghe, T.; Ravichandran, K. S.; Vandenabeele, P. Cancer cells dying from ferroptosis impede dendritic cell-mediated anti-tumor immunity. *Nat. Commun.* **2022**, *13*, 3676.
[57] Yang, K.; Wang, X. K.; Song, C. H.; He, Z.; Wang, R. X.; Xu, Y. R.; Jiang, G. Y.; Wan, Y.; Mei, J.; Mao, W. J. The role of lipid metabolic reprogramming in tumor microenvironment. *Theranostics* **2023**, *13*, 1774–1808.
[58] Cao, Z. Y.; Li, D. D.; Zhao, L.; Liu, M. T.; Ma, P. Y.; Luo, Y. L.; Yang, X. Z. Bioorthogonal *in situ* assembly of nanomedicines as drug depots for extracellular drug delivery. *Nat. Commun.* **2022**, *13*, 2038.
[59] Italia, K.; Colah, R.; Ghosh, K. Hydroxyurea could be a good clinically relevant iron chelator. *PLoS One* **2013**, *8*, e82928.
[60] Saha, P.; Xiao, X.; Li, Y. Q.; Golonka, R. M.; Abokor, A. A.; Yeoh, B. S.; Vijay-Kumar, M. Distinct iron homeostasis in C57BL/6 and Balb/c mouse strains. *Physiol. Rep.* **2020**, *8*, e14441.
[61] Fernández-Mariño, I.; Anfray, C.; Crecente-Campo, J.; Maeda, A.; Ummarino, A.; Teijeiro-Valiño, C.; Blanco-Martinez, D.; Mpambani, F.; Poul, L., Devalliere, J. et al. Mannose-modified hyaluronic acid nanocapsules for the targeting of tumor-associated macrophages. *Drug Deliv. Transl. Res.* **2023**, *13*, 1896–1911.
[62] Zhang, P. P.; Li, B. H.; Chen, Q. F.; Wang, H.; Feng, Q. Glucose restriction induces ROS-AMPK-mediated CTR1 expression and increases cisplatin efficiency in NSCLC. *Cancer Lett.* **2022**, *543*, 215793.
[63] Teh, C. E.; Robbins, A. K.; Henstridge, D. C.; Dewson, G.; Diepstraten, S. T.; Kelly, G.; Febbraio, M. A.; Gabriel, S. S.; O' Reilly, L. A.; Strasser, A. et al. MCL-1 is essential for survival but dispensable for metabolic fitness of FOXP3^{+} regulatory T cells. *Cell Death Differ.* **2020**, *27*, 3374–3385.
[64] Mehta, P. P.; Dhapte-Pawar, V. TPGS functionalized carriers: An emerging approach for pulmonary drug delivery. In *Pulmonary Drug Delivery Systems: Material and Technological Advances*. Mehta, P. P.; Dhapte -Pawar, V., Eds.; Springer: Singapore, **2023**; pp 281–318.
[65] Pavlova, N. N.; Thompson, C. B. The emerging hallmarks of cancer metabolism. *Cell Metab.* **2016**, *23*, 27–47.